Decadal Evolution of the Nansen Ice Shelf, Antarctica, from Historical Aerial Photography and Landsat Imagery

Yujie Bian[1,2], Yuan Cheng[1,3*], Philip Christopher Reid[4]

[1] Institute for the Conservation of Cultural Heritage, School of Cultural Heritage and Information Management, Shanghai University, Shanghai, China, 200444 – bianyujie@shu.edu.cn, chengyuan@shu.edu.cn
[2] School of Mechanics and Engineering Science, Shanghai University, Shanghai, China,200444 – bianyujie@shu.edu.cn
[3] Key Laboratory of Silicate Cultural Relics Conservation (Shanghai University), Ministry of Education – chengyuan@shu.edu.cn
[4] The Marine Biological Association (MBA), The Laboratory Plymouth, UK – pchrisreid@googlemail.com

Keywords: Nansen Ice Shelf, remote sensing detection, ice shelf dynamics.

Abstract

Antarctic ice shelves regulate ice sheet mass balance through their "buttressing effect", with major implications for global sea level rise. This study focuses on the Nansen Ice Shelf in Victoria Land, East Antarctica, which exhibits complex topography and sensitivity to environmental changes. Previous research has primarily centered on its significant collapse event in 2016; however, systematic evolutionary patterns over longer timescales remain unclear. This study integrates multi-source remote sensing observations from 1948 to 2025 to systematically reconstruct changes in the Nansen Ice Shelf's geometric characteristics (crevasse width, area) and dynamic parameters (ice flow velocity). Findings reveal distinct activity differences between the northern and southern regions of the ice shelf, closely linked to their respective boundary conditions and structural features.

1. Introduction

With ongoing global warming, accelerating sea-level rise has emerged as a pressing global issue (Elneel et al., 2024) . Recent satellite observations reveal that mass loss from the Antarctic ice sheet is intensifying and has become the dominant contributor to current sea-level rise, as well as a major source of uncertainty in future projections (Li et al., 2024) . As vital floating extensions of the Antarctic ice sheet, Antarctic ice shelves constitute a critical component of the polar climate system. Through their "buttressing effect" on inland ice flows, they influence the ice sheet's mass balance and global sea level rise (Bassis et al., 2024; Goldberg et al., 2009) . The stability and dynamic evolution of ice shelves serve as sensitive indicators of climate change, responding to complex interactions between atmospheric, oceanic, and glacial processes (Pattyn et al., 2018) . Understanding the long-term evolution of ice shelves is therefore essential for improving predictions of future sea-level rise and refining models of cryospheric response to climate change.

Advances in remote sensing, particularly the availability of multi-decadal satellite archives, have substantially improved our understanding of ice shelf dynamics. These datasets enable detailed analyses of changes in ice flow velocity, crevasse propagation, and calving behavior, revealing ice shelf responses to both short-term disturbances and long-term forcings (Zhao et al., 2024) . However, many previous studies are event-centered or limited to short observational periods, hindering a comprehensive understanding of ice shelf evolution over longer timescales. Ice shelf stability is governed not by single processes but by the interplay of internal dynamics operating across multiple temporal scales (Pattyn et al., 2018) . Thus, uncovering the mechanisms underlying ice shelf evolution necessitates integrating multi-source datasets and performing long-term, spatiotemporal analyses. Such an approach is essential for detecting critical state transitions that may be masked by short-term variability.

The Nansen Ice Shelf (Figure 1) is located in Victoria Land, East Antarctica, within Terra Nova Bay, adjacent to the northern edge of the Drygalski Ice Tongue (Li et al., 2016) . Its unique geographic position subjects its dynamic evolution to the combined influence of regional katabatic winds, ocean circulation, and sea ice conditions. Most recent studies have focused on the dramatic calving event that occurred in 2016. Satellite remote sensing and hydroacoustic analyses have revealed the fracture propagation leading up to the calving and identified a storm-driven hydrofracturing mechanism (Dziak et al., 2018; Moctezuma-Flores and Parmiggiani, 2016) . Other investigations attribute this instability to complex basal topography and structural weaknesses (Dow et al., 2024, 2018) . However, these efforts are largely event-centric and do not capture the long-term evolution of the ice shelf, leaving its multi-decadal dynamics poorly understood.

This study uses multi-decadal, multi-source remote sensing data to reconstruct the long-term dynamic evolution and stability transitions of the Nansen Ice Shelf. By quantitatively analyzing key geometric and dynamic indicators — including ice shelf area, fracture widening, and ice flow velocity — we reveal its decadal-scale evolution. Our findings highlight south-north heterogeneity in shelf area changes, nonlinear growth of critical fractures from quiescent to accelerated stages, and exponential increases in ice flow velocity prior to collapse — hallmarks of systemic destabilization.

2. Data

To enable robust long-term analysis of the Nansen Ice Shelf, this study collected multi-source satellite imagery covering the region from 1948 to 2025. This comprehensive dataset supports the reconstruction of the ice shelf's geometry and dynamic characteristics.

2.1 Remote Sensing Data

The dataset consists of historical aerial photographs and Landsat satellite imagery spanning 1948-2025 (Table 1). For the pre -1972 period, two declassified historical black-and-white aerial photographs acquired in 1948 (covering the Relief Inlet and Mount Melbourne regions) were utilized to reconstruct pre-satellite ice shelf conditions. These photographs, originally acquired by the U.S. Navy and sourced from the U.S. Geological Survey (USGS) Earth Resources Observation and Science (EROS) Center, were scanned and georeferenced, yielding a spatial resolution of approximately 121-128 m. Additionally, to capture the ice shelf state in 1963, we incorporated Declassified Intelligence Satellite Photographs (DISP) from the ARGON mission. From 1972 onward, continuous Landsat observations were employed: starting with MSS sensors on Landsat 1-3 (60-80 m resolution); followed by TM sensors on Landsat 4-5 (30 m, 7 bands); ETM+ on Landsat 7 (including a 15 m panchromatic band); and finally, high-quality OLI imagery from Landsat 8-9. All Landsat data were obtained at the L1TP processing level to ensure geometric consistency across the entire time series.

Data	Temporal Coverage	Spatial Resolution	Number of Images	Source	Data Format
Historical Aerial Photographs	1948	121-128m	2	USGS (EROS)	GeoTIFF
ARGON DISP	1963	~140 m (Vector)	1	USGS	Shapefile
Landsat-1 MSS	1972-1974	60 m	5	USGS	GeoTIFF
Landsat-4 TM	1982-2012	30 m	19	USGS	GeoTIFF
Landsat-5 TM	1982-2012	30m	19	USGS	GeoTIFF
Landsat-7 ETM+	1999-2022	15 m	23	USGS	GeoTIFF
Landsat-8 OLI L1GT	2013-2025	15 m	13	USGS	GeoTIFF
Landsat-9 OLI L1GT	2013-2025	15 m	13	USGS	GeoTIFF

Table 1. Remote sensing images used for ice shelf observation

2.2 Ice Flow Velocity Data

Ice flow velocity is a fundamental indicator for evaluating the dynamic state of the Nansen Ice Shelf. To ensure temporal consistency and data reliability over the full study period, we adopted two processing strategies corresponding to different observational eras. All velocity products were derived from NASA's MEaSUREs (Making Earth System Data Records for Use in Research Environments) ITS_LIVE (Inter-mission Time Series of Land Ice Velocity and Elevation) dataset (Gardner et al., 2025). This product derives regional ice surface velocity fields by applying automated feature-tracking algorithms to overlapping optical and radar image pairs. Due to larger uncertainties in the standard products for the early period, image-pair fields were reconstructed independently.

For the pre-2010 period, due to large uncertainties in the standard ITS_LIVE annual velocity products for this region, we performed independent reconstructions. We downloaded all raw image-pair velocity products covering the Nansen Ice Shelf from the ITS_LIVE data portal (Gardner et al., 2022) . These image pairs provide temporally sporadic and spatially irregular velocity fields derived from historical aerial photography and early Landsat imagery. To ensure data quality, we applied a systematic, multi-step filtering and reconstruction workflow, including error-threshold screening, visual quality assessment, and temporal aggregation. This process yielded high-quality, annual velocity mosaics tailored to the study domain.

Unlike the earlier period, the annual ITS_LIVE velocity mosaics from 2011 onward exhibit stable performance and are deemed reliable for this region. We therefore directly employed the official ITS_LIVE annual products, which are generated by integrating multi-source satellite observations and provided at a 120 m spatial resolution. Pixel-scale spatial consistency checks between the reconstructed early-period fields and the official ITS_LIVE mosaics confirmed strong agreement, ensuring comparability across the two time-series datasets and enabling robust multi-decadal analyses.

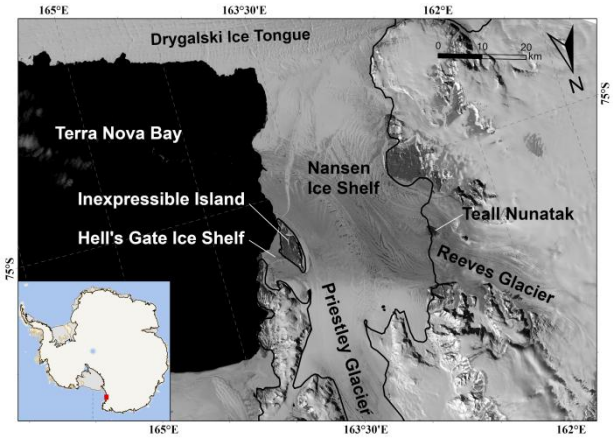

Figure 1. Study area map of the Nansen Ice Shelf and surrounding features.

3. Methodology

The Nansen Ice Shelf was divided into northern and southern sectors for independent analysis, reflecting its inherent structural and dynamic heterogeneity. The shelf is formed by the convergence of the Reeves and Priestley glaciers, creating a central north-south suture zone. The southern flank is dynamically influenced by the adjacent Derzhavinsky Ice Tongue, whereas the northern flank is stabilized by grounding at Inexpressible Island. This spatial partitioning allows us to isolate contrasting responses to external environmental forcing.

Using multi-temporal remote sensing data, we conducted long-term monitoring of the ice shelf's evolution. Our analysis focuses on two key aspects: (1) geometric changes — specifically ice shelf area and key crevasse widening — to evaluate structural degradation; and (2) variations in ice flow velocity along representative flowlines to assess dynamic responses.

3.1 Delineating Ice Shelf Fronts and Quantifying Area Change

Based on a multi-source remote sensing dataset spanning 1948-2025, we manually delineated the calving front of the

Nansen Ice Shelf to reconstruct its long-term spatial evolution and ensure accurate boundary identification. For the year 1963, the ice shelf front was directly adopted from existing coastline vector data extracted from the DISP ARGON imagery. Image preprocessing was tailored to the characteristics of different periods: imagery from 1974 and earlier, which was prone to significant spatial distortion, underwent geometric correction using high-precision Antarctic geodetic control points, followed by reprojection to the WGS84 Antarctic Polar Stereographic coordinate system. Imagery from 1972 onward already met geometric accuracy requirements and was only reprojected to ensure temporal consistency across the dataset, forming a robust basis for subsequent area analyses.

To quantify long-term area changes, we applied the Open-Box Method. Rectangular analysis boxes were established at the southern and northern margins of the ice shelf (Figure 2a), each with three closed sides and one open boundary facing the ocean. This configuration allowed changes in ice shelf extent — due to advance or calving to be directly reflected in the effective area within the box. The box positions were fixed throughout the study period. For each time step, ice-covered pixels within the boxes were extracted based on delineated front positions, and areas were computed separately for the northern, southern, and combined regions. These time series were subsequently compared with crevasse evolution and ice flow velocity data to reveal spatially differentiated ice shelf dynamics.

3.2 Monitoring of Key Ice Shelf Rifts

To quantify the structural evolution of the Nansen Ice Shelf, we systematically identified and tracked the long-term behavior of its three major rifts (Rifts 1-3). This analysis was based on the Landsat image archive, processed using the same geometric correction and reprojection protocols as those applied for front-line delineation. Rift boundaries were manually delineated through visual interpretation of high-resolution, contrast-enhanced imagery.

Crevasse widening was quantified by defining two transects along the northern and southern sectors of the ice shelf (Figure 3a), with positions aligned to flowlines discernible in the Landsat series. Annual crevasse widths were measured as the distance between corresponding points on opposite sides of each rift along the direction of ice flow. This approach minimizes the influence of fracture curvature and complex geometries, providing a reliable indicator of tensile opening. The resulting time series spans 1989-2025 and allows for detailed characterization of crevasse dynamics across regions and time.

3.3 Ice Flow Velocity Dynamics Analysis

Based on reconstructed historical velocity fields and modern ITS_LIVE annual products, we defined two flowline-aligned velocity profiles in the northern and southern sectors of the Nansen Ice Shelf to examine spatial and temporal variations in ice dynamics (Figure 4a). Velocity values along each profile were extracted at a fixed interval of 120 m, matching the spatial resolution of the ITS_LIVE dataset. To characterize ice shelf frontal dynamics, we further established a 10 km landward buffer zone from the calving front. The mean velocity of all grid cells within this zone was calculated for each time step, producing a continuous long-term velocity time series for both regions.

4. Results

4.1 Spatio-Temporal Dynamics of Ice Shelf Area

Clear spatial heterogeneity is observed in the area changes of the Nansen Ice Shelf (Figure 2b). The southern region exhibits highly dynamic behavior, with repeated episodic fluctuations. Between 1948 and 2015, it underwent 12 localized calving events, each resulting in area losses of 3%-8%, with intervals as short as 1.5 years — indicative of a persistently unstable, cyclic adjustment regime. By contrast, the northern region shows a slower, linear growth trend over multi-decadal scales, reflecting a higher degree of structural resilience. Although temporary retreats occurred during the mid-1960s to early 1970s and again in 2016, the northern sector subsequently entered recovery phases following each collapse.

From a temporal evolution perspective, the Nansen Ice Shelf’s history can be divided into three main phases, separated by two key disturbances (Figure 2b). The first disturbance occurred during a sustained retreat from the mid-1960s to the early 1970s. This nearly decade-long event had a profound impact on the entire ice shelf, though its effects differed between the northern and southern regions. In the northern sector, despite substantial area loss, a rapid recovery began immediately after the retreat, initiating four decades of continuous growth that peaked at 923 km² in 2015. In contrast, for the inherently dynamic southern sector, this retreat represented a deeper, longer-lasting phase within its natural calving cycle without altering its fundamental “advance-calve” behavior.The second disturbance was the major collapse event of 2016. During this event, the southern region lost approximately 68 km², which still fell within its historical fluctuation range. The northern region, however, lost about 125 km² — nearly 50% of its total area at that time — abruptly ending four decades of stability. Crucially, unlike the earlier cycle, the northern region failed to recover after this collapse and instead entered a new regime of low-amplitude, unpredictable fluctuations, with its area stabilizing between 875 and 885 km².

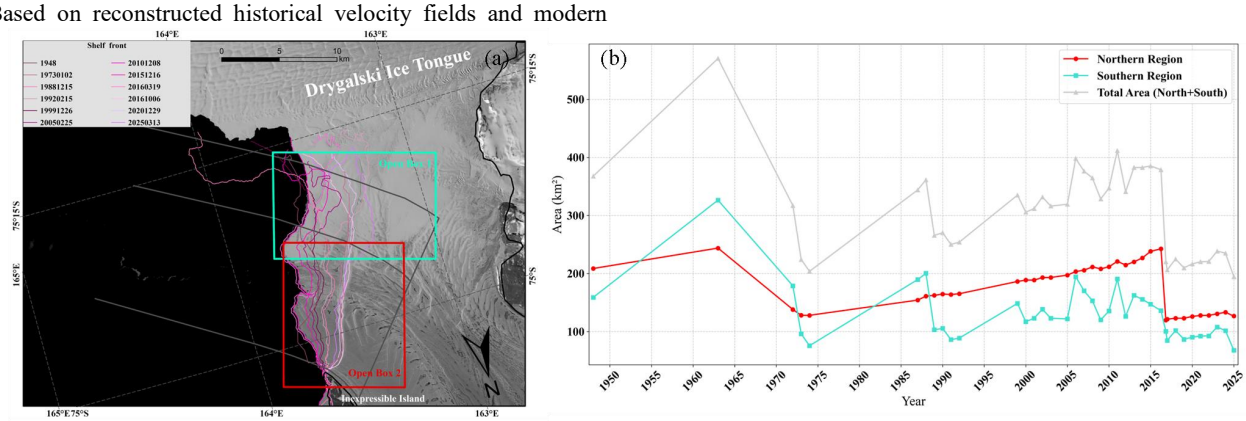

Figure 2. Spatiotemporal evolution of the Nansen Ice Shelf front and area from 1948 to 2025.

(a) Map of the Nansen Ice Shelf showing selected calving front positions between 1948 and 2025. The cyan (Open Box 1) and red (Open Box 2) rectangles indicate the northern and southern regions, respectively, used for separate area analysis. (b) Time series of area change for the northern region (red line), southern region (cyan line), and total area (gray line) from 1948 to 2025. The area was calculated within the corresponding open boxes shown in (a).

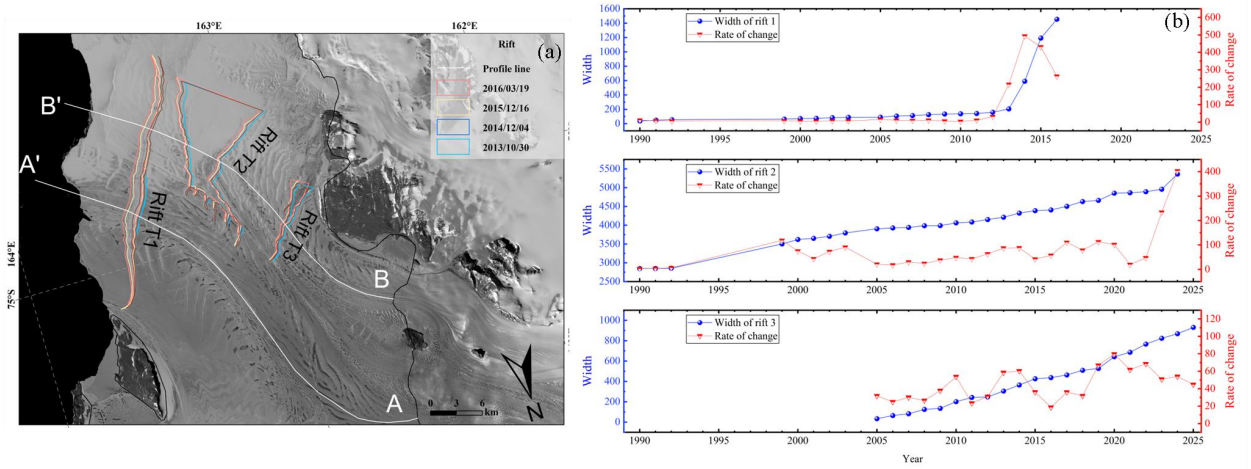

Figure 3. Long-term evolution of major rifts on the Nansen Ice Shelf.

(a) Satellite image showing the location of the three major rifts (Rift 1, 2, and 3) on the Nansen Ice Shelf. Colored polygons show the progressive widening of Rift 2 in selected years. White lines (A-A' and B-B') indicate the velocity profiles. (b) Time series of the width (blue line, left y-axis) and rate of change (red line, right y-axis) for Rift 1, Rift 2, and Rift 3 from top to bottom, respectively. The width was measured along profiles oriented with the ice flow direction.

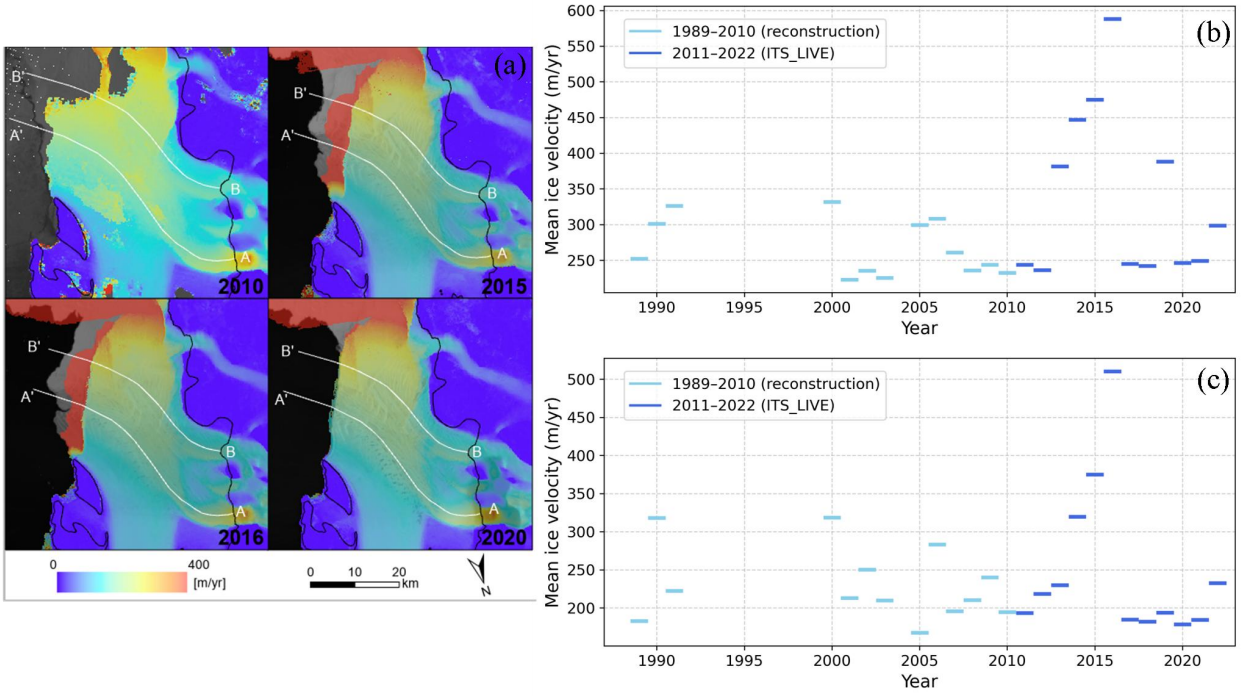

Figure 4. Ice dynamics of the Nansen Ice Shelf from 1989 to 2022.

(a) Ice velocity maps of the Nansen Ice Shelf for selected years (2010, 2015, 2016, and 2020). (b) and (c) show the time series of mean ice velocity for the southern and northern regions, respectively, from 1989 to 2022. Velocity is averaged within a 10-km buffer zone extending inland from the calving front. Light blue indicates reconstructed data (1989-2010), and dark blue indicates ITS_LIVE data (2011-2022).

4.2 Temporal Development of Major Ice Shelf Rifts

Monitoring the evolution of the three major rifts (Rifts 1, 2, and 3) on the Nansen Ice Shelf from 1990 to 2025 shows that Rifts 2 and 3 consistently exhibited high-speed, linear expansion over the entire period, without signs of significant acceleration (Figure 3a). In contrast, Rift 1 underwent a marked transition

This contribution has been peer-reviewed. The double-blind peer-review was conducted on the basis of the full paper.
https://doi.org/10.5194/isprs-annals-XI-2-2026-891-2026 | © Author(s) 2026. CC BY 4.0 License.

from a long-term dormant state to a phase of rapid, uncontrolled widening.

Rift 1, located within the relatively stable northern sector of the Nansen Ice Shelf, exhibited a distinct two-stage evolution characterized by a transition from a prolonged dormant state to a phase of rapid, runaway expansion, with 2012 marking the critical tipping point (Figure 3b). From 1990 to 2012, the rift widened at an exceptionally slow average rate of just 8.4 m/yr, increasing in width from 5 m to only 15 m over 12 years — substantially slower than contemporaneous rift growth in the southern region, and with negligible interannual variability. Following 2012, Rift 1 abruptly entered an exponential growth phase. Its average annual widening rate surged to 128 m/yr — over 15 times the pre-2012 rate — and continued to accelerate, reaching 142 m/yr by 2015. During this short interval, its width expanded from 15 m to 179 m. This explosive expansion critically destabilized the northern ice shelf structure, providing direct precursors to the large-scale calving event in 2016.

Rifts 2 and 3, both located in the inherently dynamic southern sector of the Nansen Ice Shelf, exhibited a consistent high-speed expansion over the long term (Figure 3b). Rift 2 maintained a persistently rapid widening rate, averaging approximately 42.3 m/yr between 1990 and 2025. Although minor interannual variability was observed (ranging from 38.5 to 45.8 m/yr), no distinct acceleration or deceleration phases occurred. Over this period, its width expanded steadily from 12 m to 114 m, eventually triggering a minor calving event in 2024. Rift 3 displayed a similar evolution, with an average annual widening rate of 37.6 m/yr from 1990 to 2025, increasing in width from 9 m to 98 m. While its rate was marginally lower than that of Rift 2, it likewise showed no evidence of systematic acceleration.

4.3 Ice Flow Velocity Time-Series Analysis

Based on reconstructed and observed data spanning 1989 to 2022, the average ice flow velocity in the northern and southern marginal zones of the Nansen Ice Shelf exhibits distinct temporal variability.

The southern region (Figure 4b) exhibited fluctuating ice flow velocities throughout the study period. Between 1989 and 2010, velocities ranged primarily between 230 and 330 m/yr, characterized by several oscillation cycles. From 2011 to 2022, the velocity continued to fluctuate within a similar range. For example, the average velocity in 2015 was approximately 250 m/yr, and following the 2016 calving event, it remained nearly unchanged at ~245 m/yr in 2017, indicating no significant stepwise acceleration or deceleration associated with the collapse.

The ice flow velocity in the northern region (Figure 4c) displayed marked phased variability. From 1989 to 2011, velocities remained relatively low, fluctuating between 180 and 240 m/yr. Beginning in 2012, the flow entered a phase of sustained acceleration, culminating in a peak of over 500 m/yr in early 2016. Following the 2016 collapse event, velocities abruptly declined to approximately 180 m/yr. During the subsequent period (2017-2022), flow rates gradually recovered from this minimum and stabilized within the range of 180-230 m/yr.

A strong dynamic correlation is observed between ice flow velocity and ice shelf area in the northern sector before and after the 2016 collapse event (Figure 5). In the years leading up to the collapse (approximately 2012-2016), the ice flow velocity exhibited a pronounced acceleration trend, coinciding with a gradual increase in ice shelf area. This culminated in a historical peak of over 500 m/yr in early 2016. In 2016, when the ice shelf underwent a sharp area loss, the flow velocity simultaneously dropped from its peak to approximately 190 m/yr. Thereafter, both variables entered a new steady state: the ice shelf area stabilized at a post-collapse low, while the flow velocity fluctuated at levels significantly below its pre-collapse maximum.

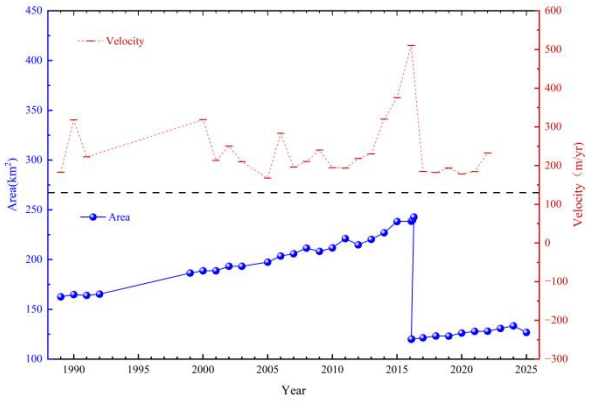

Figure 5. Relationship between ice velocity and area change in the northern region of the Nansen Ice Shelf.

5. Conclusions

This study reconstructs the geometric and dynamic evolution of the Nansen Ice Shelf from 1948 to 2025, revealing decadal-scale spatial heterogeneity. The southern sector shows persistent high-frequency mass fluctuations, acting as the primary zone of adjustment, while the northern sector, buttressed by Inexpressible Island, has long served as a structural anchor. However, this structural stability is not permanent. Rift 1 remained dormant for over two decades before entering a phase of exponential widening in 2012. This nonlinear transition critically weakened the northern sector and directly contributed to the large-scale collapse in 2016. Ice flow velocity exhibited a strong precursor signal, accelerating significantly from 2012 to a historical peak in 2016, then rapidly declining post-collapse — further confirming the coupling between flow dynamics and structural integrity.

In conclusion, the 2016 event was not isolated, but the result of systemic destabilization driven by delayed fracture expansion and internally amplified by dynamic feedback. This underscores the importance of long-term, high-resolution monitoring to detect critical transitions in ice shelf stability.

Building upon these observational findings, our follow-on work will focus on investigating the underlying physical mechanisms driving these state transitions. Future research will integrate the reconstructed multi-decadal kinematic records with numerical ice-sheet models to quantify the stress field variations and fracture mechanics leading up to the 2016 collapse. Additionally, incorporating oceanographic and atmospheric datasets — such as basal melt rates, ocean temperature anomalies, and surface mass balance — will be crucial for unraveling the complex ice-ocean-atmosphere interactions that govern both the long-term stability and the post-collapse evolutionary trajectory of the Nansen Ice Shelf.

This contribution has been peer-reviewed. The double-blind peer-review was conducted on the basis of the full paper.
https://doi.org/10.5194/isprs-annals-XI-2-2026-891-2026 | © Author(s) 2026. CC BY 4.0 License.

Acknowledgements

This research was supported by the National Natural Science Foundation of China (No. 42301149) and the International Cooperation Project of the State Administration of Foreign Experts Affairs (No. H20240329).

References

Bassis, J. N., Crawford, A., Kachuck, S. B., Benn, D. I., Walker, C., Millstein, J., Duddu, R., Åström, J., Fricker, H. A., Luckman, A., 2024. Stability of ice shelves and ice cliffs in a changing climate. Annual Review of Earth and Planetary Sciences, 52, 221–247.https://doi.org/10.1146/annurev-earth-040522-122817.

Dow, C. F., Lee, W. S., Greenbaum, J. S., Greene, C. A., Blankenship, D. D., Poinar, K., Forrest, A. L., Young, D. A., Zappa, C. J., 2018. Basal channels drive active surface hydrology and transverse ice shelf fracture. Science Advances, 4, eaao7212. https://doi.org/10.1126/sciadv.aao7212.

Dow, C. F., Mueller, D., Wray, P., Friedrichs, D., Forrest, A. L., McInerney, J. B., Greenbaum, J. S., Blankenship, D. D., Lee, C. K., Lee, W. S., 2024. The complex basal morphology and ice dynamics of the Nansen Ice Shelf, East Antarctica. The Cryosphere, 18, 1105–1123. https://doi.org/10.5194/tc-18-1105-2024.

Dziak, R. P., Lee, W. S., Yun, S., Lee, C.-K., Haxel, J. H., Lau, T.-K., Matsumoto, H., Roche, L., Tepp, G., 2018. The 2016 Nansen Ice Shelf calving event: Hydroacoustic and meteorological observations of ice shelf fracture and iceberg formation. In: 2018 OCEANS - MTS/IEEE Kobe Techno-Oceans (OTO), IEEE, Kobe, pp. 1–7. https://doi.org/10.1109/OCEANSKOBE.2018.8559076.

Elneel, L., Zitouni, M. S., Mukhtar, H., Galli, P., Al-Ahmad, H., 2024. Exploring key aspects of sea level rise and their implications: An overview. Water, 16, 388. https://doi.org/10.3390/w16030388.

Gardner, A. S., Fahnestock, M. A., Scambos, T. A., 2022.MEaSUREs ITS_LIVE Landsat image-pair glacier and ice sheet surface velocities, version 1. NASA National Snow and Ice Data Center Distributed Active Archive Center (DAAC) data set IMR9D3PEI28U.

Gardner, A. S., Greene, C. A., Kennedy, J. H., Fahnestock, M. A., Liukis, M., López, L. A., Lei, Y., Scambos, T. A., Dehecq, A., 2025. ITS_LIVE global glacier velocity data in near real time. EGUsphere, 2025, 392. https://doi.org/10.5194/egusphere-2025-392.

Goldberg, D., Holland, D. M., Schoof, C., 2009. Grounding line movement and ice shelf buttressing in marine ice sheets. Journal of Geophysical Research: Earth Surface, 114,F04026. https://doi.org/10.1029/2008JF001227.

Li, R., Li, G., Hai, G., Xie, H., Cheng, Y., Chen, W., Cui, X., Ding, M., Gao, C., Hao, T., Ke, C., Li, C., Li, J., Liu, Y., Ran, J., Ren, J., Shen, Q., Shen, Y., Shi, H., Wang, S., Wang, Z., Zhan, J., Zhang, B., Zhong, M., Zhou, C., 2024. Reconciled estimation of Antarctic ice sheet mass balance and contribution to global sea level change from 1996 to 2021. Science China Earth Sciences, 67, 3562–3578. https://doi.org/10.1007/s11430-023-1394-5.

Li, T., Ding, Y., Zhao, T., Cheng, X., 2016. Iceberg calving from the Antarctic Nansen Ice Shelf in April 2016 and its local impact. Science Bulletin, 61, 1157–1159. https://doi.org/10.1007/s11434-016-1124-9.

Moctezuma-Flores, M., Parmiggiani, F., 2016. SAR observations of the Nansen Ice Shelf fracture. European Physical Journal Plus, 131, 384. https://doi.org/10.1140/epjp/i2016-16384-y.

Pattyn, F., Ritz, C., Hanna, E., Asay-Davis, X., DeConto, R., Durand, G., Favier, L., Fettweis, X., Goelzer, H., Golledge, N. R., Kuipers Munneke, P., Lenaerts, J. T. M., Nowicki, S., Payne, A. J., Robinson, A., Seroussi, H., Trusel, L. D., Van Den Broeke, M., 2018. The Greenland and Antarctic ice sheets under 1.5 °C global warming. Nature Climate Change, 8, 1053–1061. https://doi.org/10.1038/s41558-018-0305-8.

Zhao, A., Cheng, Y., Fraser, A. D., Bennetts, L. G., Xiao, H., Liang, Q., Li, T., Li, R., 2024. Long-term evolution of the Sulzberger Ice Shelf, West Antarctica: Insights from 74-year observations and 2022 Hunga-Tonga volcanic tsunami-induced calving. Earth and Planetary Science Letters, 646, 118958. https://doi.org/10.1016/j.epsl.2024.118958.